Modeling and Numerical Analysis of Graphene Microbeam Resonator

by

Yerkebulan Yessetov

Submitted to the Department of Mathematics
in partial fulfillment of the requirements for the degree of

Master of Science in Applied Mathematics

at the

NAZARBAYEV UNIVERSITY

July 2023

Author .....
Department of Mathematics

Certified by .....
Piotr Skrzypacz
Associate Professor
Thesis Supervisor

Accepted by .....
Gonzalo Hap Hortelano
Dean, School of Sciences and Humanities

Modeling and Numerical Analysis of Graphene Microbeam Resonator

by

Yerkebulan Yessetov

Submitted to the Department of Mathematics
on , in partial fulfillment of the
requirements for the degree of
Master of Science in Applied Mathematics

Abstract

Microelectromechanical systems (MEMS) have emerged as a revolutionary technology, enabling the development of miniaturized devices with diverse functionalities and superior performance. Among the essential components of MEMS, microresonators hold significant importance as they find applications in various fields, including mass and force sensing, molecular detection, and nanoscale imaging. The quest to improve the sensitivity and performance of microresonators has led researchers to explore novel materials and innovative designs.

This thesis delves into the static and dynamic behavior of graphene cantilever beam resonators under electrostatic actuation at their free tips. A rigorous analysis of the system's response was performed. The constitutive nonlinear equation of the system was derived using the Energy method and Hamilton's principle. An analytical solution to the nonlinear static problem was obtained.

A lumped mass model was developed to study the essential dynamics of the graphene cantilever beam. The generalized stiffness coefficient for the beam under load at its tip was calculated, enabling a comprehensive analysis of its dynamic behavior. A key focus was on investigating the dynamic pull-in conditions of the system under both constant and harmonic excitation. Analytical predictions were validated through numerical simulations. We observed that the system exhibited periodic solutions when the excitation parameters α and λ were below a certain separatix curve, leading to sustained oscillations. On the other hand, if these parameters exceeded the separatix curve, the system experienced pull-in instability, causing the beam to collapse. Furthermore, we explored the impact of excitation frequency on the dynamic response of the graphene cantilever beam under harmonic load. The simulations revealed that choosing the excitation frequency near the beam's resonant frequency could lead to structural collapse under certain parameter conditions.

Thesis Supervisor: Piotr Skrzypacz
Title: Associate Professor

Acknowledgements

I would like to express my deepest gratitude to my thesis supervisor, Professor Piotr Skrzypacz, for his invaluable guidance, support, and encouragement throughout this research journey. His expertise, patience, and unwavering dedication have been instrumental in shaping this work and enhancing its quality.

I am also immensely grateful to my family for their constant love, understanding, and encouragement. To my wife, Nadira, thank you for your unwavering support, understanding, and sacrifices. Your presence and belief in me have been a constant source of motivation. To my son, Ak-Tore, thank you for bringing joy and inspiration to my life, even during the most challenging times.

Contents

List of Figures

Chapter 1

Introduction

Microelectromechanical systems (MEMS) have revolutionized numerous fields by enabling the creation of miniaturized devices with remarkable performance and functionalities. MEMS devices are distinguished by their compact size, low power consumption, and ability to integrate mechanical, electrical, and optical features on a single chip [32]. Among the vital components of MEMS are microresonators that are excited near their resonance frequencies. These microresonators find extensive applications in mass and force sensors, including the detection of proteins [7], molecules [11], electrons, and nanoparticles [25]. However, the sensitivity of these sensors can be improved by addressing the weight of the microbeam, as the minimum detectable quantity is often limited by the mass of the resonator. Therefore, lightweight and high-strength materials are highly desirable to overcome this limitation.

In this context, graphene has emerged as a promising material for MEMS and microresonators due to its light weight and outstanding mechanical properties, such as high Young's modulus and tensile strength. Table 1.1 shows the summary of graphene's mechanical characteristics compared to common MEMS components as steel and silicon.

Graphene is a single layer of carbon atoms tightly bound together. The superior properties of graphene stem from its carbon-carbon bond structure and sp^2 hybridization [5]. This unique arrangement gives graphene remarkable mechanical properties, including a high Young's modulus of 2 TPa [16] and a failure strength that is sig-

material	Young's modulus (GPa)	Tensile strength (GPa)
Graphene	2000 ± 400 [16]	130 ± 10 [15]
Steel	200 [3]	0.25 [9]
Silicon	$130 - 169$ [8]	7 [31]

Table 1.1: Mechanical properties of graphene, steel and silicon.

nificantly greater than that of the strongest steel [17]. It also grants it remarkable ductility, making it stretchable by up to 20% [26]. Its possible uses span several areas, such as the creation of transparent electrodes, ultra-strong composites, and flexible, stretchable screens for display or energy storage purposes [14].

Interestingly, though graphene was not originally thought to exhibit piezoelectric properties due to its symmetry, recent advancements have enabled its application in the field of micro and nano-electromechanical systems (MEMS/NEMS). This could enable the development of new energy harvesting, actuation, and transduction technologies [28]. Furthermore, graphene's high sensitivity and low mass make it an ideal candidate for high-resolution mass sensing, and its high thermal conductivity suggests potential use as a thermal management material [6]. Its thermal conductivity at room temperature equals to $500 W m^{-1} K^{-1}$ [2].

It is worth to mention the importance of graphene's adhesion energy with substrates for the stable, long-term operation of micro and nano-devices. Furthermore, the exceptional tribological properties of graphene make it beneficial for reducing friction and offering protection against corrosion [10, 14].

Graphene's remarkable attributes offer opportunities for further miniaturization of MEMS resonators and have led to a new wave of research in this area. Utilizing graphene resonators in mass detection has become a particularly compelling topic of study. For example, in [4] it has been found that nonlinear vibrations can enhance the sensitivity of graphene microbeam resonator. Natsuki et al. employing the continuum elasticity theory, have shown that the mass sensors with double-layered graphene sheets (DLGSs) provide higher sensitivity compared to single-layered graphene sheets (SLGSs) [19]. Another way to increase the detection sensitivity has been studied in [13]. The study associates it with the increase in the magnetic field that results in

sensor's frequency shift. There are great number of works studying potential applications of graphene microresonators through experimental results. However, we are interseted in mathematical analysis of such systems.

For instance, Wei et al. investigated the steady-state behavior of a graphene Euler beam subjected to a constant load and provided analytical and finite element solutions [29]. The use of Rayleigh-Ritz method with Hermite cubic interpolation yielded approximate finite element solutions, which were validated against analytical solutions.

Several studies have investigated the dynamic behavior of electrostatically actuated systems made of graphene. Among the notable research works are [1, 12, 23, 30, 20]. Electrostatic actuation is widely preferred in the field of microelectromechanical systems due to its simplicity and efficiency, offering advantages over alternative actuation methods such as electrothermal, piezoelectric, and electromagnetic actuation [27, 32]. When electrostatically actuated resonators are employed, the electric load applied to a cantilever beam comprises both AC and DC components. The DC component induces deflection of the beam to its equilibrium position, while the AC component generates vibrations around this equilibrium position. The equilibrium position is attained when the restoring force of the beam matches the electrostatic force [32].

However, if the DC polarization voltage is increased beyond a certain threshold, exceeding the restoring force, the beam continues to deflect until it contacts an adjacent structure or surface, resulting in collapse. This phenomenon is known as the "pull-in" instability, and the threshold voltage at which it occurs is referred to as the "pull-in voltage".

Pull-in can be classified into two types: static pull-in and dynamic pull-in. Static pull-in describes the occurrence of pull-in solely due to DC actuation, while dynamic pull-in can arise from AC harmonic excitation or the motion of the structure [32].

Analyzing and understanding pull-in is essential in the design of MEMS resonators. It is crucial to tune the electric load parameters to avoid the pull-in instability, as it can lead to structural collapse and device failure.

Skrzypacz et al. [23] conducted a comprehensive investigation, providing the necessary and sufficient conditions for the existence of periodic solutions for a lumped mass model subjected to a constant DC voltage. This study contributed valuable insights into the dynamic behavior of the model under a constant loading scenario.

Additionally, the pull-in phenomenon of the same lumped mass model, but excited by a harmonic load, was explored in two separate research works: [12] and [20]. In [20], Omarov et al. employed Sturm's theorem to identify periodic solutions of the lumped mass model with general initial conditions, and their analytical results were verified through numerical simulations implemented in the Python programming language.

Furthermore, the work of Anjum et al. [1] and Wei et al. [30] delved into the study of the nonlinear graphene beam equation and the existence of several natural frequencies of the system. These studies utilized the variational iteration method based on Laplace transform and the Pade technique to obtain approximate solutions.

This thesis investigates the static and dynamic behavior of a graphene cantilever beam subjected to electrostatic actuation at its free tip. The same oscillator model proposed in [24] is employed, comprising low-mass graphene beam of length ℓ, an inflexible platform acting as a movable electrode attached to the free end of the beam, and a fixed electrode covered with a dielectric layer of thickness h and dielectric constant ε_r, as shown in Fig. 1-1. The potential difference and gap between the two electrodes are represented by V and d respectively.

The interaction of attractive electrostatic force due to the potential difference and the nonlinear restoring force of the beam is expected to lead to high-frequency oscillations.

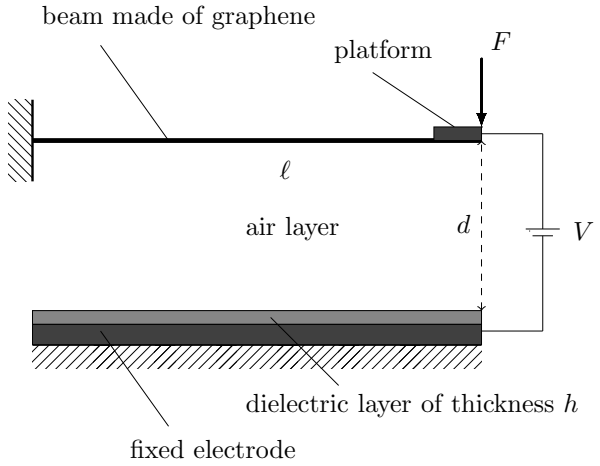

Figure 1-1: A schematic of graphene microresonator.

The study is structured as follows: In Chapter 2, the constitutive nonlinear equation governing the system is derived using the Energy method and Hamilton's principle, and boundary conditions are established. In Chapter 3, an analytical solution for the static problem is computed. Chapter 4 presents the development of a lumped mass model, which is employed to study the fundamental dynamics of the system, and also provides the calculation of the generalized stiffness coefficient for the graphene cantilever beam under the load at its tip. The pull-in phenomenon under both constant and harmonic excitation is analyzed in Chapter 5. Simulation results for dynamic pull-in and resonance are presented in Chapter 6. Finally, the thesis concludes with Chapter 7.

Chapter 2

Mathematical model

This section focuses on the derivation of the constitutive nonlinear equation for a cantilever beam made of graphene by employing Hamilton's principle, an essential concept in variational mechanics.

2.1 Constitutive stress-strain equation for graphene

It is theoretically and experimentally justified that the stress-strain relationship for the the classical Euler-Bernoulli beam made of graphene can be written as

$$\sigma = E\varepsilon + D|\varepsilon|\varepsilon, \tag{2.1}$$

where σ, ε, E are the stress, strain and Young's modulus and $D = -E^2/4\sigma_{max}$ the second-order elastic stiffness constant [15, 18]. The negative value of D is associated with a reduced stiffness at high tensile strains and increased stiffness at high compressive strains. The values of E and D were determined by [15] through the measurement of deformation in single-atomic-layer graphene sheets using nanoindentation with an atomic force microscope. The experimental findings yielded a value of E as $340 \pm 40 Nm^{-1}$ and D as $-690 \pm 120 Nm^{-1}$.

According to [15], the nonlinearity of the stress-strain response of graphene arises from the third-order term of a strain-dependent energy potential expressed as a Taylor

series. This characterization of the stress-strain behavior of graphene will be utilized in the forthcoming modeling section.

2.2 Model equation for Euler-Bernoulli beam made of graphene

Here we consider a cantilever beam subjected to a force applied at the free end (see Figure 2-1), and a small segment on the beam before and after deflection would be analyzed (see Figure 2-2).

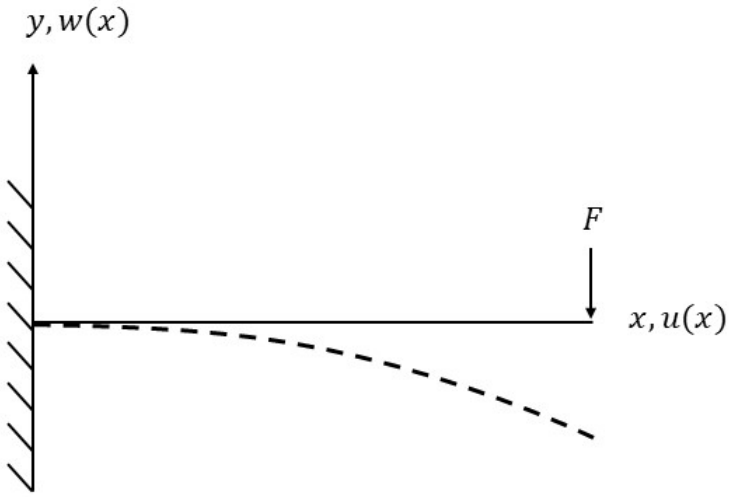

Figure 2-1: A schematic of a deflected beam under a point load at the free tip

According to the Euler-Bernoulli beam theory, the cross section of the beam remains plane and perpendicular to the beam's centerline [32]. To analyze the behavior of the beam, it is necessary to determine the axial strain at a specific point, denoted as point B, located at a distance y from the centerline, see Figure 2-2. In the given figure, the axial displacement of point B caused by pure bending is represented as u_b, and it is expressed as

$$u_b = -yw'. \tag{2.2}$$

The axial strain ε_b can be calculated as

$$\varepsilon_b = \frac{\partial u_b}{\partial x} = -yw''. \tag{2.3}$$

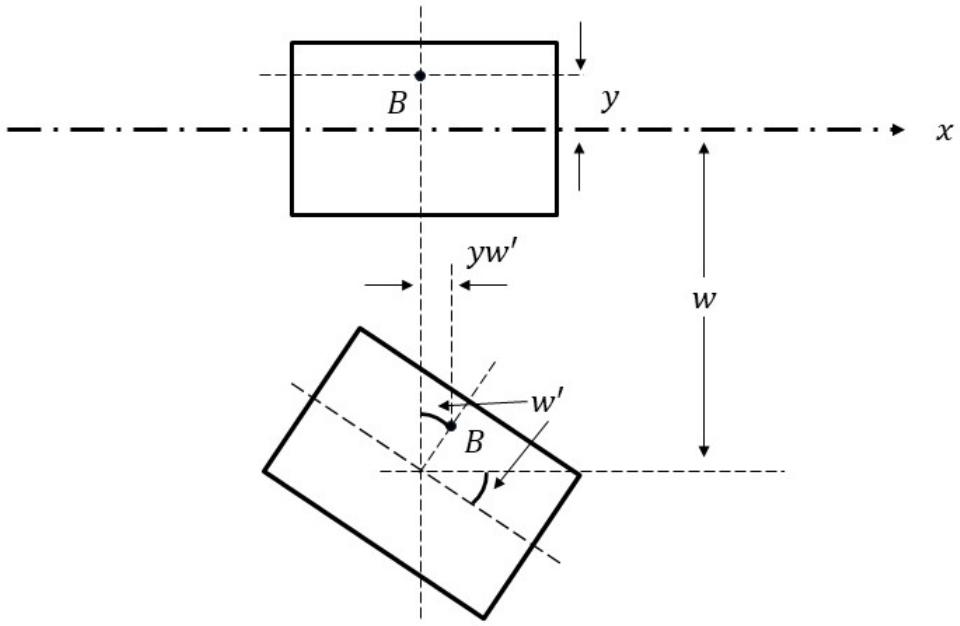

Figure 2-2: A segment of a beam before and after bending

By integrating the stress-strain equation (2.1) with respect to strain, we obtain the strain energy density, which represents the energy stored per unit volume in the material. This energy density is a measure of the potential energy stored within the beam due to deformation. Integrating this quantity over the entire volume of the beam allows us to determine the total potential energy of the system. Thus, we get

$$U = \frac{1}{2}E\varepsilon\varepsilon^{\mathcal{T}} + \frac{1}{3}D|\varepsilon|\varepsilon\varepsilon^{\intercal}, \tag{2.4}$$

where U is the strain energy density, and $\varepsilon = (\varepsilon_x, \varepsilon_y, \varepsilon_z, \gamma_{xy}, \gamma_{xz}, \gamma_{yz})$ is the strain, where $\varepsilon_x = \frac{\partial u}{\partial x}$, $\varepsilon_y = \frac{\partial w}{\partial y}$, $\varepsilon_z = \frac{\partial v}{\partial z}$, $\gamma_{xy} = \frac{1}{2}\left(\frac{\partial u}{\partial y} + \frac{\partial w}{\partial x}\right)$, $\gamma_{xz} = \frac{1}{2}\left(\frac{\partial u}{\partial z} + \frac{\partial v}{\partial x}\right)$, $\gamma_{yz} = \frac{1}{2}\left(\frac{\partial w}{\partial z} + \frac{\partial v}{\partial y}\right)$ are the strain components. For the Euler-Bernoulli beam, it is assumed

that

$$\varepsilon_x = \frac{\partial u}{\partial x} = -yw'' = \varepsilon_b, \tag{2.5}$$

and

$$\varepsilon_y = \varepsilon_z = \gamma_{xy} = \gamma_{xz} = \gamma_{yz} = 0. \tag{2.6}$$

Therefore, Eq. (2.4) simplifies to

$$U = \frac{1}{2}E\varepsilon_x^2 + \frac{1}{3}D|\varepsilon_x|\varepsilon_x^2. \tag{2.7}$$

Then, the total potential energy E_{pot} can be expressed as

$$E_{pot} = \frac{1}{2}\int_V E\varepsilon_x^2\, dV + \frac{1}{3}\int_V D|\varepsilon_x|\varepsilon_x^2\, dV. \tag{2.8}$$

Inserting the axial strain into Eq. (2.8) yields

$$\begin{aligned} E_{pot} &= \frac{1}{2}\int_V E(-yw'')^2\, dV + \frac{1}{3}\int_V D|-yw''|(-yw'')^2\, dV \\ &= \underbrace{\frac{1}{2}\int_V E(yw'')^2\, dV}_{E_{pot}^{(1)}} + \underbrace{\frac{1}{3}\int_V D|w''|(w'')^2y^3\, dV}_{E_{pot}^{(2)}}. \end{aligned} \tag{2.9}$$

Note that y is the distance from the centerline, hence it is always positive.

$$\begin{aligned} E_{pot}^{(1)} &= \frac{1}{2}\int_V E(yw'')^2\, dV = \frac{1}{2}\int_0^\ell \int_A E(yw'')^2\, dA\, dx \\ &= \frac{1}{2}\int_0^\ell E(w'')^2 \left(\int_A y^2\, dA\right) dx, \end{aligned} \tag{2.10}$$

where ℓ is the length of the beam and A is the cross-sectional area. Expressing the second moment of inertia of cross-section

$$I_1 = \int_A y^2\, dA. \tag{2.11}$$

Eq. (2.10) can be rewritten as

$$E_{pot}^{(1)} = \frac{EI_1}{2} \int_0^\ell (w'')^2 \, dx. \tag{2.12}$$

$E_{pot}^{(2)}$ is expanded in the similar manner:

$$\begin{aligned} E_{pot}^{(2)} &= \frac{1}{3} \int_V D|w''|(w'')^2 y^3 \, dV = \frac{1}{3} \int_0^\ell \int_A D|w''|(w'')^2 y^3 \, dA \, dx \\ &= \frac{1}{3} \int_0^\ell D|w''|(w'')^2 \left(\int_A y^3 \, dA \right) dx = \frac{DI_2}{3} \int_0^\ell |w''|(w'')^2 \, dx, \end{aligned} \tag{2.13}$$

where

$$I_2 = \int_A y^3 \, dA \tag{2.14}$$

is the third moment of inertia of cross-section.

Inserting Eq. (2.12) and Eq. (2.13) into Eq. (2.9) gives the following potential energy equation

$$E_{pot} = \frac{EI_1}{2} \int_0^\ell (w'')^2 \, dx + \frac{DI_2}{3} \int_0^\ell |w''|(w'')^2 \, dx. \tag{2.15}$$

The kinetic energy of a beam can be calculated based on the mass distribution along the length of the beam and the velocity of its individual mass elements. The general formula for the kinetic energy of a beam is given by:

$$E_{kin} = \frac{\rho A}{2} \int_0^\ell \dot{w}^2 \, dx, \tag{2.16}$$

where ρ is material density and $\dot{w}$ is the time derivative of the deflection $w(x,t)$.

The work W done by the external force on the cantilever beam at the free end can be written as

$$W = Fw(\ell), \tag{2.17}$$

where $w(\ell)$ is the deflection of the beam at $x = \ell$.

2.3 Hamilton's Principle

In order to derive the graphene beam equation of motion we need to use the Lagrangian energy functional $I(w)$ and the Hamilton's principle [32]. The Lagrangian energy functional is defined by

$$\mathcal{I}(w) = E_{kin}(w) - E_{pot}(w) + W(w). \tag{2.18}$$

Applying the Hamilton's principle on the Lagrangian $I(w)$ gives

$$\int_{t_1}^{t_2} \delta\mathcal{I}(w)\, dt = \int_{t_1}^{t_2} \left(\delta E_{kin}(w) - \delta E_{pot}(w) + \delta W(w)\right)\, dt = 0, \tag{2.19}$$

where t_1 and t_2 are two moments of time during which the system experiences the variation, and δ is the variation operator. The Hamilton's principle requires calculation of the variations of the work of the external force (δW), the kinetic (δE_{kin} and potential (δE_{pot}) energies, simplifying and expressing in terms of variation displacement δw.

The variation of the kinetic energy, and the work is given as

$$\delta W = F\delta w(\ell), \tag{2.20}$$

and

$$\delta E_{kin} = \rho A \int_0^l \dot{w}\delta\dot{w}\, dx. \tag{2.21}$$

By applying integration by parts to the variation of the kinetic energy expression (2.21), we can rewrite it in terms of the virtual displacement δw as follows:

$$\begin{aligned}
\int_{t_1}^{t_2} (\delta E_{kin})\, dt &= \int_{t_1}^{t_2} \left[\rho A \int_0^{\ell} \dot{w}\delta\dot{w}\, dx\right]\, dt = \rho A \int_0^{\ell} \left[\int_{t_1}^{t_2} \dot{w}\delta\dot{w}\, dt\right]\, dx \\
&= \rho A \int_0^{\ell} \left[\underbrace{\dot{w}\delta w|_{t_1}^{t_2}}_{=0} - \int_{t_1}^{t_2} \ddot{w}\delta w\, dt\right]\, dx \\
&= \rho A \int_0^{\ell} \left[-\int_{t_1}^{t_2} \ddot{w}\delta w\, dt\right]\, dx.
\end{aligned} \tag{2.22}$$

The boundary term in time vanishes in Eq. (2.22) due to the boundary conditions imposed on the virtual displacement. Specifically, it is assumed that the virtual displacement satisfies $\delta w(t_1) = \delta w(t_2) = 0$. The variation of the potential energy E_{pot} can be written as

$$\delta E_{pot} = EI_1 \int_0^\ell w''\delta w''\, dx + DI_2 \int_0^\ell |w''|w''\delta w''\, dx. \tag{2.23}$$

To express the equation above Eq. (2.23) in terms of displacement variation δw several integration by parts need to be implemented as shown below

$$EI_1 \int_0^\ell w''\delta w''\, dx = EI_1 w''\delta w'|_0^\ell - EI_1 w'''\delta w|_0^\ell + EI_1 \int_0^\ell w''''\delta w\, dx, \tag{2.24}$$

$$\begin{aligned} DI_2 \int_0^l |w''|w''\delta w''\, dx = {} & DI_2|w''|w''\delta w'|_0^\ell - DI_2\left(|w''|w''\right)'\delta w\big|_0^\ell \\ & + DI_2 \int_0^\ell \left(|w''|w''\right)''\delta w\, dx. \end{aligned} \tag{2.25}$$

Substituting Eq. (2.24) - Eq. (2.25) into Eq. (2.19) and grouping the terms gives

$$\begin{aligned} \int_{t_1}^{t_2} \Bigg\{ \int_0^\ell \Big[-\rho A\ddot{w} - EI_1 w'''' - DI_2\left(|w''|w''\right)''\Big]\delta w\, dx - \Big[EI_1 w'' + DI_2|w''|w''\Big]\delta w'\Big|_0^\ell \\ + \Big[EI_1 w''' + DI_2\left(|w''|w''\right)' + F\Big]\delta w(\ell) - \Big[EI_1 w''' + DI_2\left(|w''|w''\right)'\Big]\delta w(0)\Bigg\}\, dt = 0. \end{aligned} \tag{2.26}$$

According to the definition the variation δw and δu are arbitrary, therefore each group of term must be zero in order to satisfy the equation Eq. (2.26), which leads to the following equation of motion and boundary conditions:

$$\rho A\ddot{w} + EI_w'''' + DI_2\left(|w''|w''\right)'' = 0, \tag{2.27}$$

$$EI_1 w''' + DI_2\left(|w''|w''\right)' = 0; \quad \text{or} \quad \delta w = 0 \quad \text{at} \quad x = 0, \tag{2.28}$$

$$EI_1 w''' + DI_2 \left(|w''|w''\right)' = -F; \quad \text{or} \quad \delta w = 0 \quad \text{at} \quad x = \ell, \tag{2.29}$$

$$EI_1 w'' + DI_2 |w''|w'' = 0; \quad \text{or} \quad \delta w' = 0 \quad \text{at} \quad x = 0, \ell. \tag{2.30}$$

Since the beam is fixed at $x = 0$, then

$$w(0) = w'(0) = 0. \tag{2.31}$$

Furthermore, Eq. (2.30) and Eq. (2.31) imply

$$EI_1 w'' + DI_2 |w''|w'' = 0 \quad \text{at} \quad x = \ell, \tag{2.32}$$

and from Eq. (2.29) we can conclude that

$$EI_1 w''' + DI_2 \left(|w''|w''\right)' = -F \quad \text{at} \quad x = \ell. \tag{2.33}$$

Chapter 3

Static problem

3.1 Analytic solution

Let $F(x) = F$ be a point load at the free end of the beam. The beam equation under the point load is expressed as follows

$$EI_1 w'''' + DI_2 \left(|w''|w''\right)'' = 0, \quad 0 < x < l, \tag{3.1}$$

subject to the boundary conditions

$$w(0) = 0, \tag{3.2}$$

$$w'(0) = 0, \tag{3.3}$$

$$\left(EI_1 + DI_2|w''|\right) w''\big|_{x=\ell} = 0, \tag{3.4}$$

$$\left(EI_1 w''' + DI_2 \left(|w''|w''\right)'\right)\big|_{x=\ell} = -F. \tag{3.5}$$

Integrating the equation (3.1) twice, and applying the boundary conditions (3.4) - (3.5), we get

$$\left(EI_1 + DI_2|w''|\right) w'' = -F(x - \ell), \quad 0 < x < l. \tag{3.6}$$

The right-hand side of the equation (3.6) is positive, which implies that the left-hand side of the equation is also positive for $F \geq 0$. Cantilever beam subjected

to a positive load F at the free tip bends down as shown in Fig. 2-1. This static response of the system is associated with concave shape of the deflection function $w(x)$. Therefore, we require w'' to be negative. Hence, (3.6) can be expressed as

$$EI_1 w'' - DI_2(w'')^2 = -F(x-\ell), \tag{3.7}$$

which yields

$$w'' = \frac{EI_1 \pm \sqrt{(EI_1)^2 - 4DI_2F(x-\ell)}}{2DI_2}. \tag{3.8}$$

The real solution of (3.8) exists only if f is small (i.e. $F \leq \frac{(EI_1)^2}{4|D|I_2 l}$).

The equation (3.8) satisfies the boundary condition (3.4) only if

$$w'' = \frac{EI_1 - \sqrt{(EI_1)^2 - 4DI_2F(x-\ell)}}{2DI_2}. \tag{3.9}$$

Integrating (3.9) once and twice gives

$$w' = \frac{EI_1}{2DI_2}x + \frac{((EI_1)^2 - 4DI_2F(x-\ell))^{\frac{3}{2}}}{12(DI_2)^2F} + C_1, \tag{3.10}$$

and

$$w = \frac{EI_1}{4DI_2}x^2 - \frac{((EI_1)^2 - 4DI_2F(x-\ell))^{\frac{5}{2}}}{120(DI_2)^3F^2} + C_1x + C_2, \tag{3.11}$$

where C_1 and C_2 are integration constants that can be found using boundary conditions (3.2) and (3.3). It follows

$$C_1 = -\frac{((EI_1)^2 + 4DI_2F\ell)^{\frac{3}{2}}}{12(DI_2)^2F}, \tag{3.12}$$

and

$$C_2 = \frac{((EI_1)^2 + 4DI_2F\ell)^{\frac{5}{2}}}{120(DI_2)^3F^2}. \tag{3.13}$$

Thus, the analytic solution of the graphene beam equation under the point load at

the tip can be written as

$$w(x) = \frac{EI_1}{4DI_2}x^2 - \frac{((EI_1)^2 - 4DI_2F(x-\ell))^{\frac{5}{2}}}{120(DI_2)^3F^2} - \frac{((EI_1)^2 + 4DI_2F\ell)^{\frac{3}{2}}}{12(DI_2)^2F}x + \frac{((EI_1)^2 + 4DI_2F\ell)^{\frac{5}{2}}}{120(DI_2)^3F^2}. \tag{3.14}$$

Note that, when D approaches zero, the analytic solution provided in (3.14) coincides with the classical deflection equation for a cantilever beam under a point load, where the beam is assumed to be a linear elastic material and that the deflection is small compared to the length of the beam. It also assumes that the load is applied perpendicular to the beam's longitudinal axis, and that the beam has a uniform cross-sectional area. The calculation is presented in Appendix.

Chapter 4

Galerkin approximation

4.1 Lumped mass model

Let's consider the deflection of the vibrating elastic beam made of graphene at the axial position $x \in [0, \ell]$ at time $t > 0$ which can be expressed as

$$\rho A \ddot{w}(t,x) + EIw''''(t,x) + DI_2 \left(|w''(t,x)|w''(t,x)\right)'' = 0, \tag{4.1}$$

with boundary and initial conditions

$$w(t,0) = 0, \tag{4.2}$$

$$w'(t,0) = 0, \tag{4.3}$$

$$\left(EI + DI_2|w''(t,\ell)|\right) w''(t,\ell) = 0, \tag{4.4}$$

$$EIw'''(t,\ell) + DI_2 \left(|w''(t,\ell)|w''(t,\ell)\right)' = -F_E, \tag{4.5}$$

and

$$w(0,x) = 0, \tag{4.6}$$

$$\dot{w}(0,x) = 0. \tag{4.7}$$

where F_E is an electrostatic Coulomb force which can be expressed as

$$F_E = \frac{\varepsilon_0 V^2 S}{2\left(d + \frac{h}{\varepsilon_r} - w(t,\ell)\right)^2}. \tag{4.8}$$

We assume that the beam has a simple geometry, and the deformation is not too large. Therefore, to study essential dynamics of the graphene beam undergoing a point force at the free tip we use one-mode Galerkin approximation

$$w(x,t) \approx X(t)Y(x), \tag{4.9}$$

where $X(t)$ is an unknown time-dependant coefficient and $Y(x)$ is a trial function that satisfies boundary condition of cantilever beam (i.e. $Y(0) = Y'(0) = 0$). First, we derive a weak formulation of the governing nonlinear differential equation (4.1) by multiplying both sides with the trial function and integrating over the interval $[0, \ell]$:

$$\begin{aligned}\int_0^\ell \rho A\ddot{w}(t,x)Y(x)\,dx + \int_0^\ell EI_1 w''(t,x)Y''(x)\,dx + \int_0^\ell DI_2\big(|w''(t,x)|w''(t,x)\big)Y''(x)\,dx \\ + \big(EI_1 w'''(t,\ell) + DI_2(|w''(t,\ell)|w''(t,\ell))'\big)Y(\ell) \\ - \big(EI_1 w''(t,\ell) + DI_2|w''(t,\ell)|w''(t,\ell)\big)Y'(\ell) = 0.\end{aligned} \tag{4.10}$$

Employing boundary conditions Eq. (4.2) - Eq. (4.5) and dividing both sides by $Y(\ell)$ yields

$$\begin{aligned}\frac{1}{Y(\ell)}\int_0^\ell \rho A\ddot{w}(t,x)Y(x)\,dx + \frac{1}{Y(\ell)}\int_0^\ell EI_1 w''(t,x)Y''(x)\,dx \\ + \frac{1}{Y(\ell)}\int_0^\ell DI_2\big(|w''(t,x)|w''(t,x)\big)Y''(x)\,dx = F_E.\end{aligned} \tag{4.11}$$

Then, the corresponding Galerkin equation for Eq. (4.11) is given as

$$\rho A\ddot{X}(t)m_1 + X(t)k_1 + |X(t)|X(t)k_2 = \frac{\varepsilon_0 V^2 S}{2\left(d + \frac{h}{\varepsilon_r} - X(t)Y(\ell)\right)^2}, \tag{4.12}$$

where

$$
\begin{aligned}
m_1 &= \frac{1}{Y(\ell)} \int_0^\ell Y^2(x)\, dx, \\
k_1 &= \frac{EI_1}{Y(\ell)} \int_0^\ell \left(Y''(x)\right)^2\, dx, \\
k_2 &= \frac{DI_2}{Y(\ell)} \int_0^\ell \left|Y''(x)\right| \left(Y''(x)\right)^2\, dx.
\end{aligned}
\tag{4.13}
$$

4.2 Dimensionless single-degree-of-freedom model

Now, let us consider a choice of $Y(x)$ for our Galerkin equation. Skrzypacz et al. [22] used the following scaled first eigenfunction for one-mode Galerkin approximation

$$
\hat{Y}(x) = \frac{1}{2}\left(\hat{Y}_3(x,\mu_1) - \frac{\hat{Y}_1(1,\mu_1)}{\hat{Y}_2(1,\mu_1)} \cdot \hat{Y}_4(x,\mu_1)\right), \tag{4.14}
$$

where

$$
\hat{Y}_1(x,\mu_1) = \cosh(\mu_1 x) + \cos(\mu_1 x), \tag{4.15}
$$

$$
\hat{Y}_2(x,\mu_1) = \sinh(\mu_1 x) + \sin(\mu_1 x), \tag{4.16}
$$

$$
\hat{Y}_3(x,\mu_1) = \cosh(\mu_1 x) - \cos(\mu_1 x), \tag{4.17}
$$

$$
\hat{Y}_4(x,\mu_1) = \sinh(\mu_1 x) - \sin(\mu_1 x), \tag{4.18}
$$

and the spectral parameter μ_1 is the first positive root of an equation

$$
1 + \cosh\mu \cos\mu = 0. \tag{4.19}
$$

$\hat{Y}(x)$ is the solution of boundary eigenvalue problem

$$
\hat{Y}''''(x) = \mu^4 \hat{Y}(x), \quad 0 < x < 1, \tag{4.20}
$$

subject to boundary conditions

$$
\hat{Y}(0) = \hat{Y}'(0) = 0 \quad \text{and} \quad \hat{Y}''(1) = \hat{Y}'''(1) = 0. \tag{4.21}
$$

However, for our Galerkin ansatz we choose $Y(x) = \hat{Y}(\frac{x}{\ell})$ for $x \in [0, \ell]$ such that

$$Y(0) = Y'(0) = 0 \quad \text{and} \quad Y''(\ell) = Y'''(\ell) = 0. \tag{4.22}$$

Now, let us compute m_1, k_1 and k_2 from Eq. (4.12). In [22] it was shown that

$$\int_0^1 \hat{Y}^2(x)\,dx = \frac{1}{4} \quad \text{and} \quad \int_0^1 \left(\hat{Y}''(x)\right)^2 dx = \mu_1^4 \int_0^1 \hat{Y}^2(x)\,dx = \frac{\mu_1^4}{4}. \tag{4.23}$$

Then, one can show that

$$\int_0^\ell Y^2(x)\,dx = \ell \int_0^1 \hat{Y}^2(x)\,dx = \frac{\ell}{4}, \tag{4.24}$$

and

$$\int_0^\ell \left(Y''(x)\right)^2 dx = \frac{1}{\ell^3} \int_0^1 \left(\hat{Y}''(x)\right)^2 dx = \frac{\mu_1^4}{4\ell^3}. \tag{4.25}$$

Employing the fact that $\hat{Y}''(x)$ is convex in $(0, 1)$ and subsequently $Y''(x)$ is convex in $(0, l)$, and $Y(l) = 1$, k_2 can be rewritten as

$$k_2 = DI_2 \int_0^\ell \left(Y''(x)\right)^3 dx, \tag{4.26}$$

see [22]. Numeric integration in Mathematica with $\mu_1 = 1.87510406871196$ gives $\int_0^1 \left(\hat{Y}''(x)\right)^3 dx = 8.02945400733$, then

$$\int_0^\ell \left(Y''(x)\right)^3 dx, = \frac{1}{\ell^5} \int_0^1 \left(\hat{Y}''(x)\right)^3 dx = \frac{1}{\ell^5}(8.02945400733). \tag{4.27}$$

Thus, we can conclude that

$$m_1 = \frac{\ell}{4}, \quad k_1 = \frac{EI_1\mu_1^4}{4\ell^3}, \quad k_2 = \frac{DI_2}{\ell^5}(8.02945400733), \tag{4.28}$$

where $\mu_1 = 1.87510406871196$ and ℓ is length of the beam.

Next, let us transform the equation Eq. (4.12) into nondimensional equation by

introducing dimensionless variables

$$\tau = \frac{t}{\ell^2}\sqrt{\frac{EI_1\mu_1^4}{\rho A}} \quad \text{and} \quad y = \frac{X}{d+\frac{h}{\varepsilon_r}}. \tag{4.29}$$

Note that

$$\ddot{X}(t) = \frac{d^2X(t)}{dt^2} = \left(d+\frac{h}{\varepsilon_r}\right)\frac{EI_1\mu_1^4}{\rho A\ell^2}\frac{d^2y(\tau)}{d\tau^2} = \left(d+\frac{h}{\varepsilon_r}\right)\frac{EI_1\mu_1^4}{\rho A\ell^2}\,\ddot{y}(\tau). \tag{4.30}$$

Substituting Eq. (4.29) into Eq. (4.12) gives

$$\left(d+\frac{h}{\varepsilon_r}\right)k_1\ddot{y} + \left(d+\frac{h}{\varepsilon_r}\right)k_1 y + \left(d+\frac{h}{\varepsilon_r}\right)k_2|y|y = \frac{\varepsilon_0 K^2 S}{2\left(d+\frac{h}{\varepsilon_r}\right)^2}\frac{1}{(1-y)^2}, \tag{4.31}$$

where K is a function of τ such that

$$K(\tau) = V\left(\tau\ell^2\sqrt{\frac{\rho A}{EI_1\mu_1^4}}\right). \tag{4.32}$$

Then, dividing the both sides of Eq. (4.31) by $\left(d+\frac{h}{\varepsilon_r}\right)k_1$ results in the following nondimensional equation that reads

$$\ddot{y} + y + \alpha|y|y = \frac{\lambda}{(1-y)^2}, \tag{4.33}$$

subject to

$$y(0) = 0, \quad \dot{y}(0) = 0, \tag{4.34}$$

where $\ddot{y}$ is the second order derivative of y with respect to τ, whereas α and λ can be expressed as

$$\alpha = \frac{k_2}{k_1}\left(d+\frac{h}{\varepsilon_r}\right) \quad \text{and} \quad \lambda(\tau) = \frac{\varepsilon_0 K^2(\tau) S}{2k_1\left(d+\frac{h}{\varepsilon_r}\right)^3}. \tag{4.35}$$

Chapter 5

Pull-in and resonance

5.1 Constant voltage

In this section, we investigate the dynamic pull-in phenomenon of the lumped mass model Eq. (4.12), considering a constant voltage applied to the cantilever beam. Our analysis is based on a phase diagram, which allows us to identify regions in the parameter space where the system exhibits periodic behavior and where pull-in occurs. Previous studies [23] have shown that the nondimensional model

$$\ddot{y} + y + \alpha|y|y - \frac{\lambda}{(1-y)^2} = 0, \tag{5.1}$$

exhibits periodic solutions for small values of $\alpha \leq 0$ and $\lambda > 0$.

To construct the phase diagram of the dimensionless equation, we need to express it in terms of the variables $\dot{y}$ and y. Therefore, we multiply both sides of Eq. (5.1) by $\dot{y}$ and integrate with respect to τ leading to the conservation of energy equation

$$\mathcal{E}(\tau) = \frac{1}{2}\left(\dot{y}(\tau)\right)^2 + \frac{1}{2}y^2(\tau) + \frac{1}{3}\alpha|y(\tau)|y^2(\tau) - \frac{\lambda}{(1-y(\tau))} = C. \tag{5.2}$$

The constant C in Eq. (5.2) is determined by applying the initial condition Eq. (4.34)

yielding $C = -\lambda$. Consequently, we can rewrite Eq. (5.2) as follows:

$$(\dot{y})^2 = -y^2 - \frac{2}{3}\alpha|y|y^2 + \frac{2\lambda}{(1-y)} - 2\lambda. \tag{5.3}$$

Next, we focus on the phase diagram, which plays a crucial role in understanding the system's dynamics. The periodic solutions of Eq. (5.1) correspond to closed curves or loops in the phase diagram, known as limit cycles. These limit cycles appear when the right-hand side of Eq. (5.3) has a root in the interval $(0, 1)$, indicating periodic behavior. In contrast, when there are no roots in this interval, pull-in occurs.

Of particular importance is the curve, that separates the regions with different dynamics of the system, known as separatix. If the initial conditions of the system lie inside the separatix, the solution is periodic; otherwise it is not periodic [32].

In order to determine the range of positive parameter values of α and λ that lead to periodic solutions, we need to analyze the separatix, which occurs when the horizontal axis is tangent to the right-hand side of Eq. (5.3) within the interval $(0, 1)$. Let us denote this function as $f_{\alpha,\lambda}(y)$. Then $f_{\alpha,\lambda}(y)$ can be expressed as:

$$f_{\alpha,\lambda}(y) = -y^2 - \frac{2}{3}\alpha y^3 + \frac{2\lambda}{(1-y)} - 2\lambda = \frac{y\left(\frac{2}{3}\alpha y^3 - \left(\frac{2}{3}\alpha - 1\right)y^2 - y + 2\lambda\right)}{1-y}. \tag{5.4}$$

Note that Eq. (5.4) has at most four roots. One root is negative and lies outside the interval $(0, 1)$, while another root occurs at $y = 0$. The remaining two roots exist within the interval $(0, 1)$. Moreover, the cubic function

$$h_{\alpha,\lambda}(y) = \frac{2}{3}\alpha y^3 - \left(\frac{2}{3}\alpha - 1\right)y^2 - y + 2\lambda \tag{5.5}$$

intersects the horizontal axis at the same points as $f_{\alpha,\lambda}(y)$, except for zero. Eq. (5.5) is tangent to the horizontal axis if both $h_{\alpha,\lambda}(y^*) = 0$ and $h'_{\alpha,\lambda}(y^*) = 0$ for some $y^* \in (0, 1)$. Then,

$$h'_{\alpha,\lambda}(y) = 2\alpha y^2 - 2\left(\frac{2}{3}\alpha - 1\right)y - 1 = 0 \tag{5.6}$$

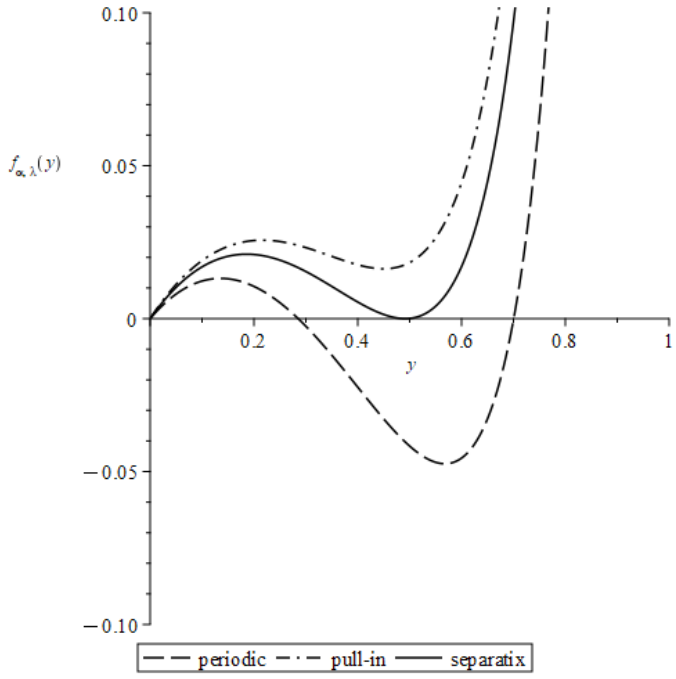

Figure 5-1: The separatix occurs when the potential function $f_{\alpha,\lambda}(y)$ is tangent to the horizontal axis.

yields

$$y^*_{1,2} = \frac{\left(\frac{2}{3}\alpha - 1\right) \pm \sqrt{\left(\frac{2}{3}\alpha - 1\right)^2 + 2\alpha}}{2\alpha}, \tag{5.7}$$

where only

$$y^* = \frac{\left(\frac{2}{3}\alpha - 1\right) + \sqrt{\left(\frac{2}{3}\alpha - 1\right)^2 + 2\alpha}}{2\alpha} \tag{5.8}$$

lies within the interval $(0, 1)$. Consequently, the system exhibits an oscillatory or periodic solution if $h_{\alpha,\lambda}(y^*) \leq 0$ for some positive parametric values of α and λ. This condition can be expressed as:

$$h_{\alpha,\lambda}(y^*) = \frac{1}{162\alpha^2}\left(-8\alpha^3 + \alpha(27 - 6\nu) - 9(-3 + \nu) - 2\alpha^2(9 + 2\nu - 162\lambda)\right) \leq 0, \tag{5.9}$$

where

$$\nu = \sqrt{9 + 6\alpha + 4\alpha^2}. \tag{5.10}$$

Rearranging the inequality and expressing λ in terms of α gives

$$\lambda \leq -\frac{1}{324\alpha^2}\left(-8\alpha^3 + \alpha\left(27 - 6\nu\right) - 9\left(-3 + \nu\right) - 2\alpha^2\left(9 + 2\nu\right)\right) = \mathcal{K}(\alpha). \tag{5.11}$$

As a result, the exact formula for dynamic pull-in voltage can be expressed as follows:

$$V_{pull-in} = \sqrt{\frac{2k_1\left(d + \frac{h}{\varepsilon_r}\right)^3 \mathcal{K}(\alpha)}{\varepsilon_0 S}}. \tag{5.12}$$

Another crucial parameter in MEMS devices is the pull-in time, which represents the time required for the system to collapse. The pull-in time can be obtained from Eq. 5.3, where we express the velocity of the beam's tip at a given position and parameter value λ as follows:

$$\dot{y} = \frac{dy}{dt} = \sqrt{-y^2 - \frac{2}{3}\alpha y^3 + \frac{2\lambda}{(1-y)} - 2\lambda}. \tag{5.13}$$

Subsequently, the pull-in time, denoted as $t_{\text{pull-in}}$, is determined by

$$t_{\text{pull-in}} = \int_0^1 \frac{dy}{\sqrt{-y^2 - \frac{2}{3}\alpha y^3 + \frac{2\lambda}{(1-y)} - 2\lambda}}. \tag{5.14}$$

The integration of this expression over the interval $[0, 1]$ corresponds to the distance that the beam's tip needs to travel in order to reach the fixed electrode, thus leading to the occurrence of pull-in phenomenon.

Using a similar approach, we can determine the period of oscillation T for our system by integrating dt from Eq. 5.13 over the interval $[0, y_{max}]$ and then multiplying the result by 2:

$$T = \int_0^{y_{max}} \frac{2dy}{\sqrt{-y^2 - \frac{2}{3}\alpha y^3 + \frac{2\lambda}{(1-y)} - 2\lambda}}. \tag{5.15}$$

Here, $y_{max} \in (0, 1)$ represents the amplitude of oscillation, which corresponds to the root of the the function $h_{\alpha,\lambda}(y)$.

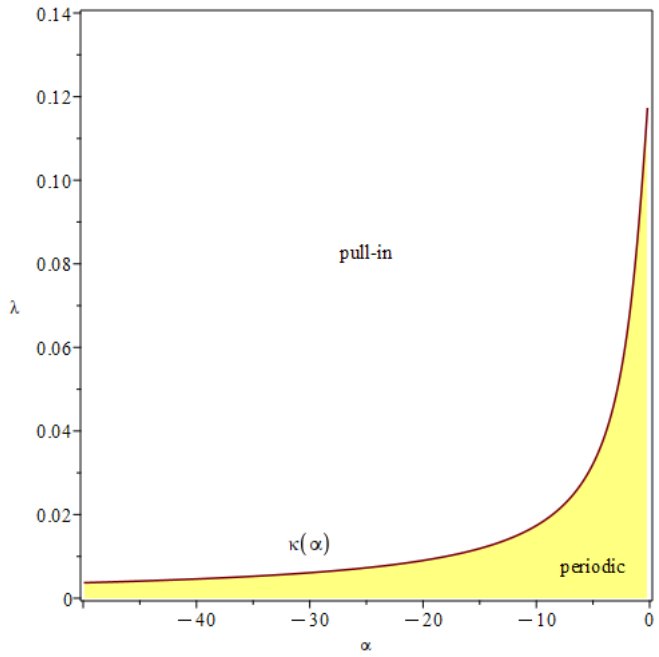

Figure 5-2: Parameter regions for pull-in and periodic solutions.

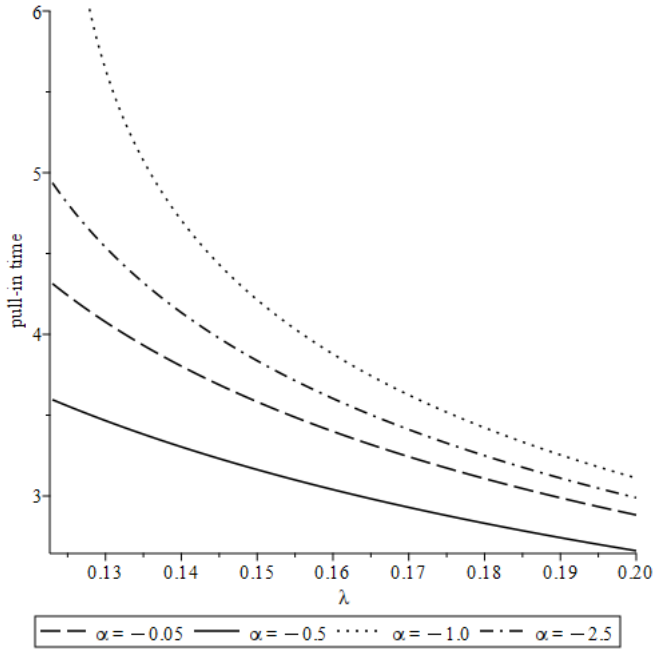

Figure 5-3: Pull-in time for different values of parameter α.

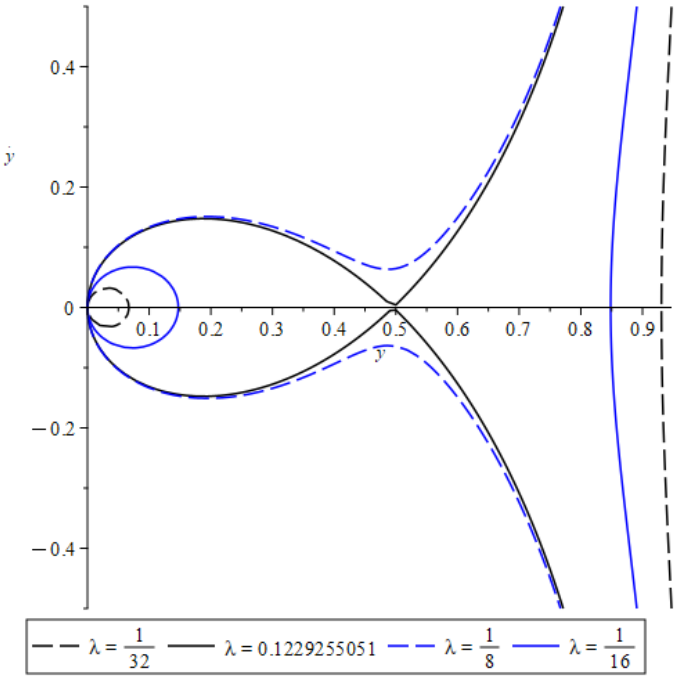

(a)

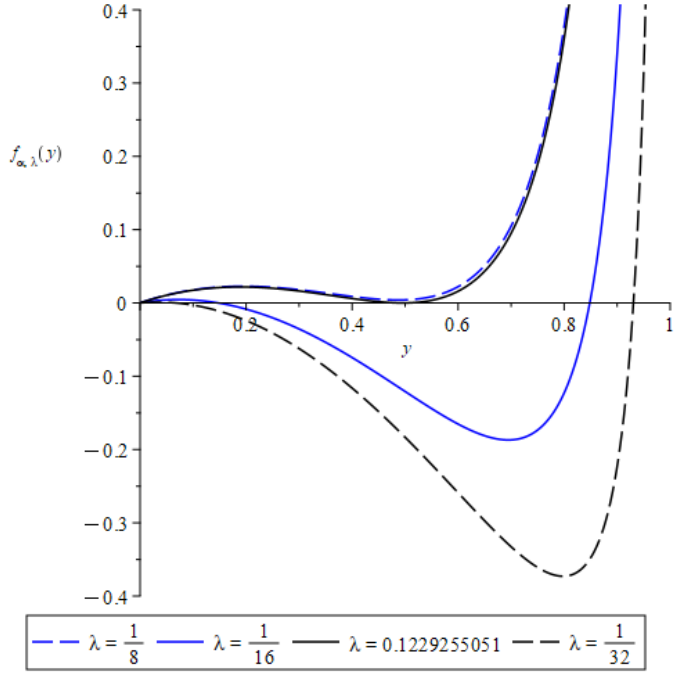

(b)

Figure 5-4: (a) Phase trajectories for $\alpha = -0.05$ and different values of λ, (b) and corresponding potential energy functions.

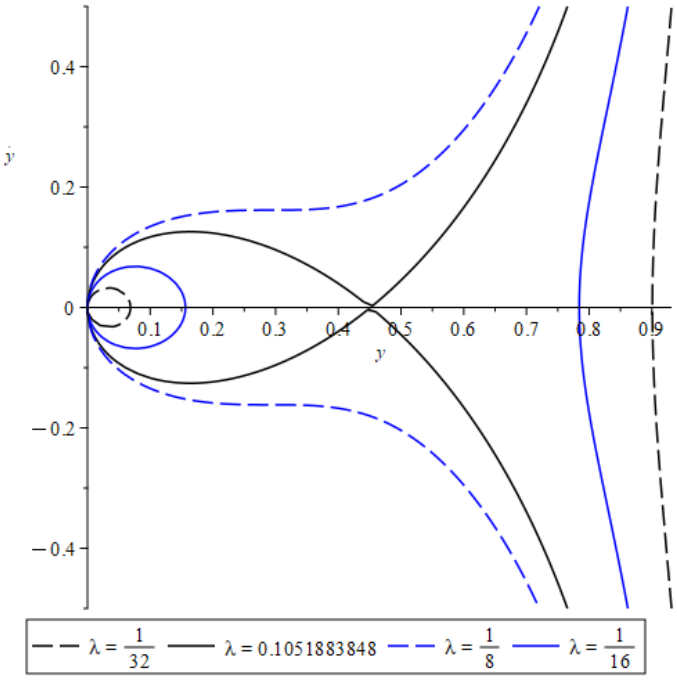

(a)

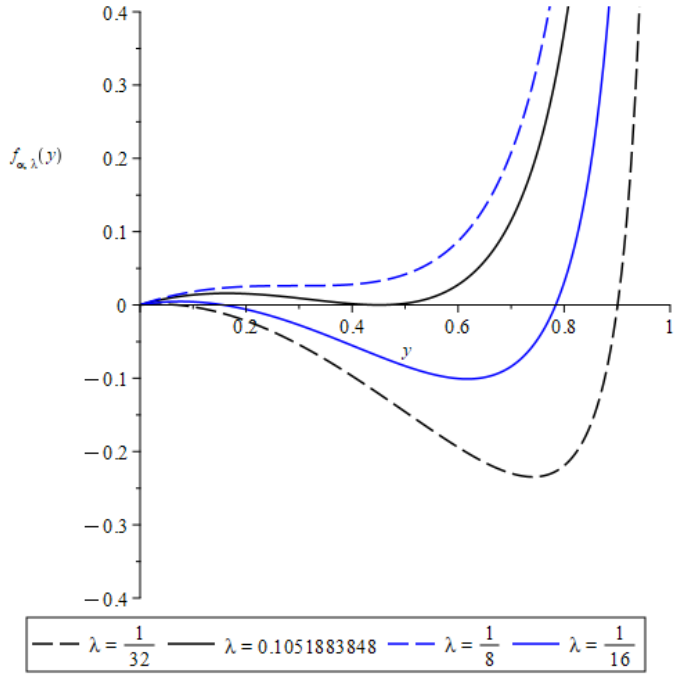

(b)

Figure 5-5: (a) Phase trajectories for $\alpha = -0.5$ and different values of λ, (b) and corresponding potential energy functions.

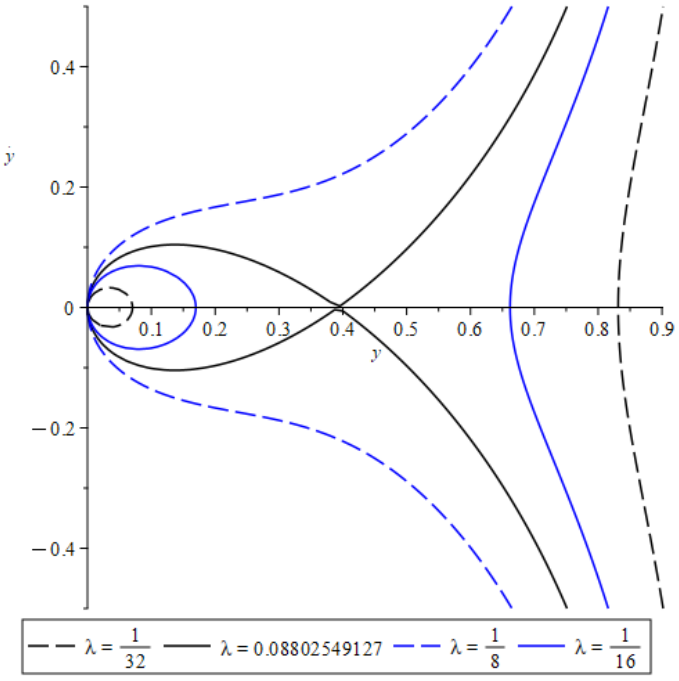

(a)

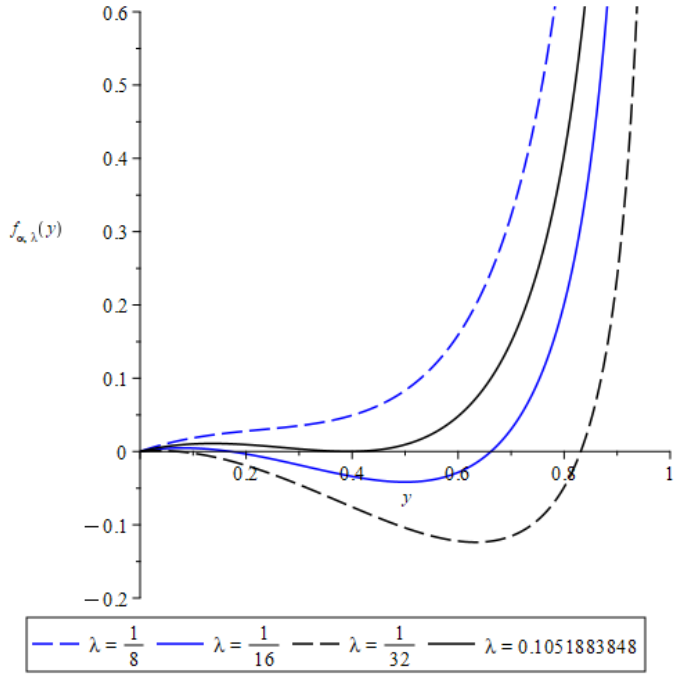

(b)

Figure 5-6: (a) Phase trajectories for $\alpha = -1.0$ and different values of λ, (b) and corresponding potential energy functions.

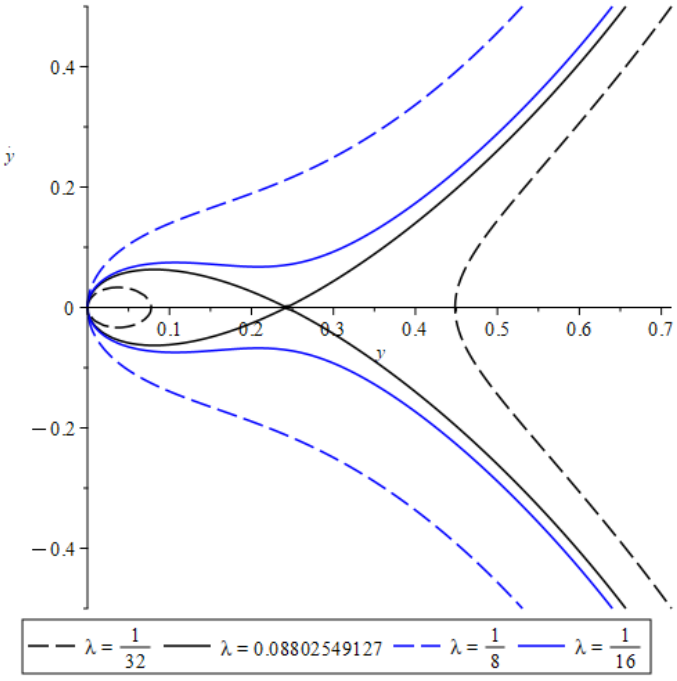

(a)

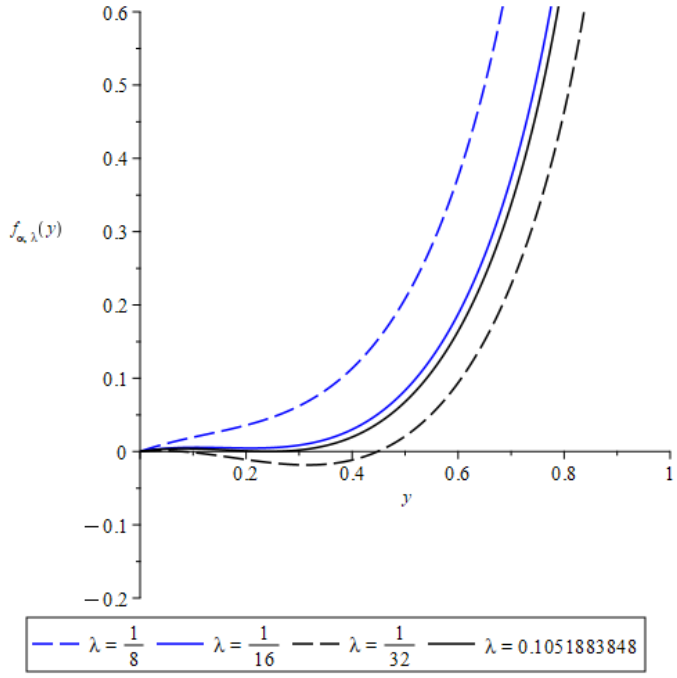

(b)

Figure 5-7: (a) Phase trajectories for $\alpha = -2.5$ and different values of λ, (b) and corresponding potential energy functions.

5.2 Time-dependent voltage

The pull-in phenomenon in microelectromechanical system (MEMS) with a parallel-plate capacitor under time-dependent voltage $V(t)$ was studied by Kadyrov et al. [12], where $V(t)$ is expressed as

$$V(t) = V_{DC} + V_{AC}\cos(\Omega t), \tag{5.16}$$

with period $T = \frac{2\pi}{\omega}$. They proposed a theorem that states the following: *for a non-negative constant c, continuous real function $h(x)$ defined on $(-\infty, 1]$, and a periodic real function $V(t)$, the second order nonlinear differential equation*

$$\ddot{y} + c\dot{y} + h(y) - \frac{V^2(t)}{(1-y)^2} = 0 \tag{5.17}$$

has a periodic solution if the equation

$$h(y) = \frac{V_M^2}{(1-y)^2} \tag{5.18}$$

has a root in $[0, 1)$, and it does not attain a periodic solution if the equation

$$h(y) = \frac{V_m^2}{(1-y)^2} \tag{5.19}$$

does not have any roots in $(-\infty, 1)$, but $h(y)$ has at least one real root within the interval $(-\infty, 1)$. Here, V_m and V_M represent the minimum and maximum amplitudes of $V(t)$, respectively, given by

$$V_m = \min_{t\geq 0}|V(t)| \quad \text{and} \quad V_M = \max_{t\geq 0}|V(t)|. \tag{5.20}$$

Our non-dimensional model (5.1) is the special case of the Eq. (5.17) with $c = 0$ and $h(y) = y + \alpha|y|y$.

To prove the existence of periodic solutions, let us denote

$$\lambda_M = \max_{\tau \geq 0} |\lambda(\tau)|. \tag{5.21}$$

According to the theorem, the second order nonlinear and non-autonomous differential equation

$$\ddot{y} + y + \alpha |y| y - \frac{\lambda(\tau)}{(1-y)^2} = 0 \tag{5.22}$$

has a periodic solution provided that

$$y + \alpha |y| y = \frac{\lambda_M}{(1-y)^2} \tag{5.23}$$

has a root in $[0, 1)$. Let us define the function $f(y)$ as

$$f_\alpha(y) = (y + \alpha |y| y)(1-y)^2. \tag{5.24}$$

Note that for $y \in [0, 1)$

$$(y + \alpha |y| y)(1-y)^2 = (y + \alpha y^2)(1-y)^2, \tag{5.25}$$

therefore,

$$f_\alpha(y) = (y + \alpha y^2)(1-y)^2 \quad \text{in} \quad [0, 1). \tag{5.26}$$

By solving $f'(y) = 0$ we can find the critical points of Eq. (5.26), that correspond to the values

$$y_{1,2} = \frac{2\alpha - 3 \pm \sqrt{4\alpha^2 + 4\alpha + 9}}{8\alpha} \quad \text{and} \quad y_3 = 1. \tag{5.27}$$

Then, using the second derivative test we can find that $f_\alpha(y)$ has a local maximum at the smallest critical point $y_1 = \frac{2\alpha - 3 + \sqrt{4\alpha^2+4\alpha+9}}{8\alpha}$ which belongs to the interval $(0, 1)$. Worth noting that $f_\alpha(y_1) > 0$ for all α. Choosing $0 < \lambda_M \leq f_\alpha(y_1) = \mathcal{K}(\alpha)$ and recalling $f_\alpha(1) = 0$, we have

$$f_\alpha(1) - \lambda_M \leq f_\alpha(y) - \lambda_M \leq f_\alpha(y_1) - \lambda_M, \tag{5.28}$$

where

$$f_\alpha(1) - \lambda_M < 0 \quad \text{and} \quad f_\alpha(y_1) - \lambda_M \geq 0. \tag{5.29}$$

Hence, the Intermediate Value Theorem guarantees the existence of some y^* in $(y_1, 1) \subset [0, 1)$ such that $f_\alpha(y^*) - \lambda_M = 0$. Then, based on theorem it can be concluded that Eq. (5.1) admits a periodic solution.

In order to have an oscillatory solution the following condition for a choice of α and λ must be satisfied:

$$\lambda \leq \frac{(-3 - 6\alpha + \mu)^2(-3 + 2\alpha + \mu)(5 + 2\alpha + \mu)}{4096\alpha^3} = \mathcal{K}(\alpha), \tag{5.30}$$

with $\mu = \sqrt{9 + 4\alpha + 4\alpha^2}$.

Chapter 6

Simulation results

6.1 Constant voltage

In this section, we present numerical simulations of the normalized deflection of the beam's free tip, denoted as $y(t)$, as a function of nondimensional time t. We analyze the behavior of the periodic solution $y(t)$ under the various sets of parameters $\lambda > 0$ and $\alpha < 0$. The simulations were conducted using Maple software, and the resulting deflection profiles are illustrated in Fig. 6-1 - 6-4.

The observed trends demonstrate the dependency of the deflection amplitude, frequency, and pull-in time on the excitation parameter λ, while keeping the parameter α fixed. Specifically, an increase in the value of λ leads to a higher amplitude and longer period of deflection. Notably, the maximum deflection amplitude is attained when λ approaches the threshold value $\kappa(\alpha)$. In Fig. 6-1 - 6-4, the periodic solutions with the highest amplitude correspond to excitation value $\lambda = \kappa(\alpha) - 10^{-3}$.

Furthermore, as we decrease the value of α, there is a corresponding increase in both the amplitude and period of $y(t)$, while the parameter λ remains unchanged.

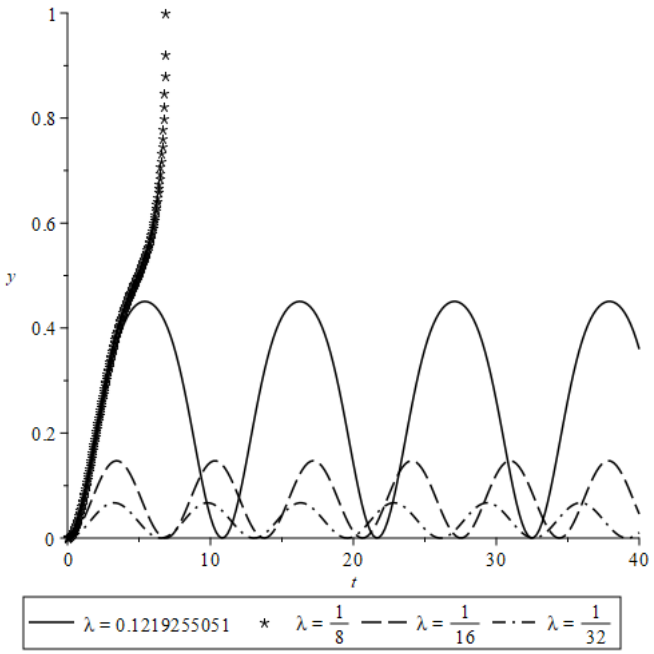

Figure 6-1: Profiles of periodic and pull-in solutions for $\alpha = -0.05$ and various values of $\lambda > 0$, $t_{\text{pull-in}} = 6.9161$.

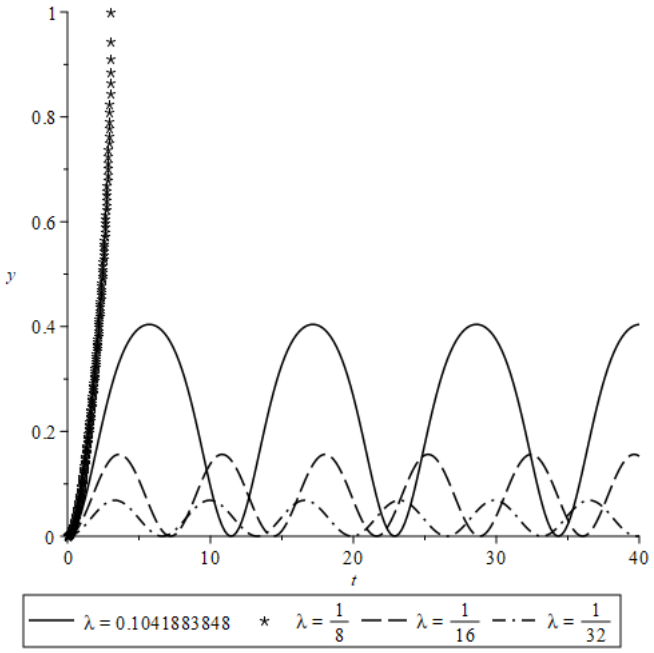

Figure 6-2: Profiles of periodic and pull-in solutions for $\alpha = -0.5$ and various values of $\lambda > 0$, $t_{\text{pull-in}} = 3.0724$.

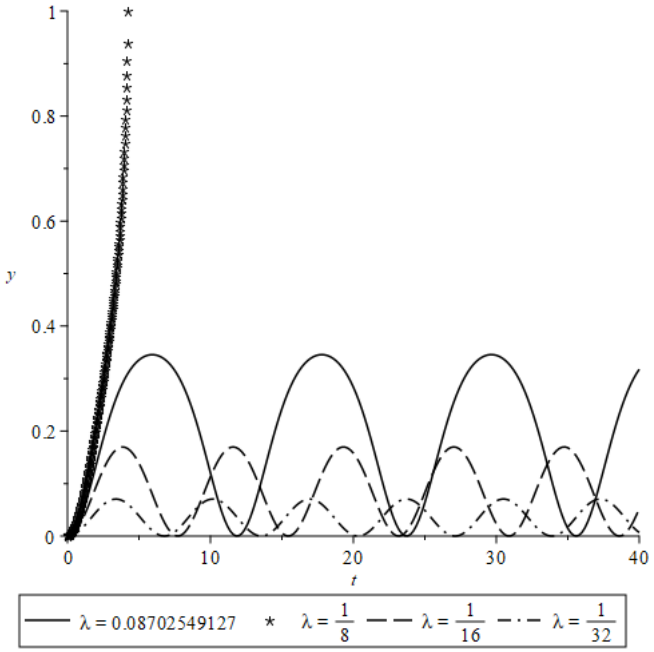

Figure 6-3: Profiles of periodic and pull-in solutions for $\alpha = -1$ and various values of $\lambda > 0$, $t_{\text{pull-in}} = 4.2412$.

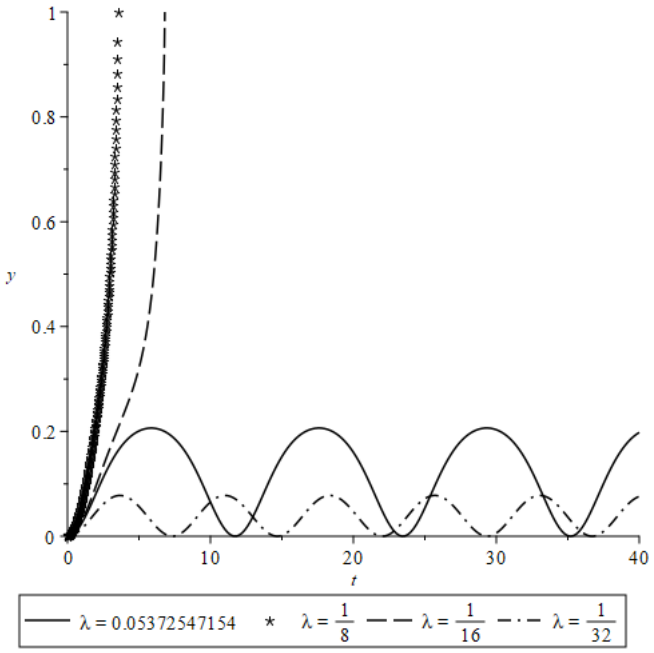

Figure 6-4: Profiles of periodic and pull-in solutions for $\alpha = -2.5$ and various values of $\lambda > 0$, $t_{\text{pull-in}} = 3.5571$ and $t_{\text{pull-in}} = 6.8102$ for $\lambda = 1/8$ and $\lambda = 1/16$, respectively.

6.2 Time-dependent voltage

In this section, we will conduct an in-depth analysis of the resonance phenomenon in a cantilever beam that is subjected to a harmonic force. Depending on the frequency of harmonic excitation the dynamic behavior of the system can be classified as primary and secondary resonance. Primary resonance refers to a dynamic behavior observed in a system when it is excited by a frequency that is close to its natural frequency. The dynamic response of the system becomes significantly amplified under primary resonance conditions, leading to large vibration amplitudes.

On the other hand, secondary resonance occurs when the system is excited at frequencies that are different from its natural frequencies and are relatively far from them [32]. However, for our analysis, we will specifically focus on primary resonance.

For our analysis we fix the value of $\alpha = -1.0$. The corresponding threshold value for excitation parameter λ^* with DC voltage V_{DC} is

$$\lambda^* = \kappa(\alpha) = 0.08802549127. \tag{6.1}$$

Recall that

$$\lambda = \frac{\varepsilon_0 V_{DC}^2 S}{2k_1\left(d + \frac{h}{\varepsilon_r}\right)^3}. \tag{6.2}$$

Let us denote

$$\beta = \frac{\varepsilon_0 S}{2k_1\left(d + \frac{h}{\varepsilon_r}\right)^3}, \tag{6.3}$$

and fix $\beta = 0.01$. Then, the corresponding pull-in voltage equals

$$V_{DC} = \sqrt{\frac{\lambda^*}{\beta}} = 2.97. \tag{6.4}$$

The pull-in value of DC voltage indicates that, for the fixed values of α and β, the system excited by harmonic force

$$V(t) = V_{DC} + V_{AC}\cos\Omega t \tag{6.5}$$

should undergo DC voltage less than pull-in voltage from Eq. (6.4). Therefore, for dynamic analysis we employ $V_{DC} = 2.5$ and $V_{AC} = 0.1$.

Using the Eq. 5.15 and utilizing the fact that

$$\omega = \frac{2\pi}{T} \tag{6.6}$$

yields natural angular frequency of the system $\omega_n = 0.7391982714$.

The results depicted in Fig. 6-5 demonstrate that when the excitation frequency Ω is selected to be close to the natural frequency ω_n, the amplitude of the graphene cantilever beam's vibration experiences a substantial increase in comparison to its behavior under constant voltage conditions.

Letting the excitation frequency to be precisely equal to the natural frequency leads to a substantial increase in the vibration amplitude of the graphene cantilever beam. However, this increment is accompanied by the occurrence of a pull-in instability scenario, wherein the free tip of the beam collapses into the fixed electrode, see Fig. 6-6.

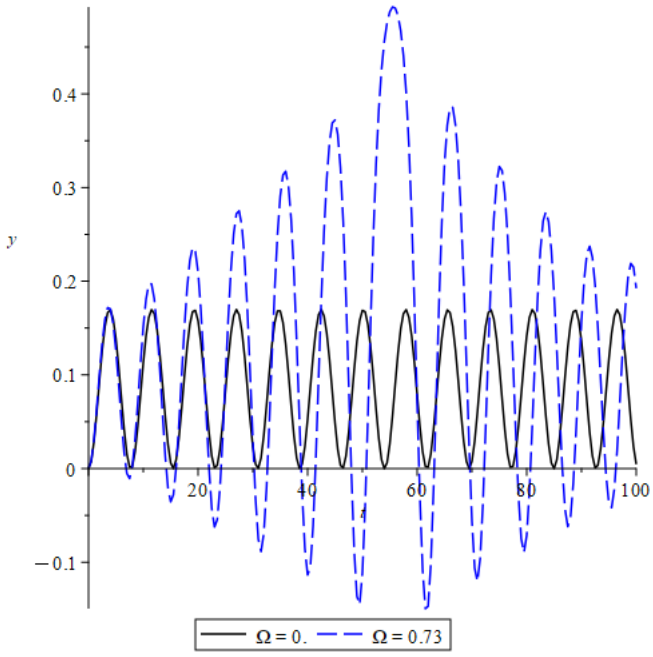

Figure 6-5: Dynamic response of graphene cantilever beam under constant voltage and harmonic excitation near natural angular frequency.

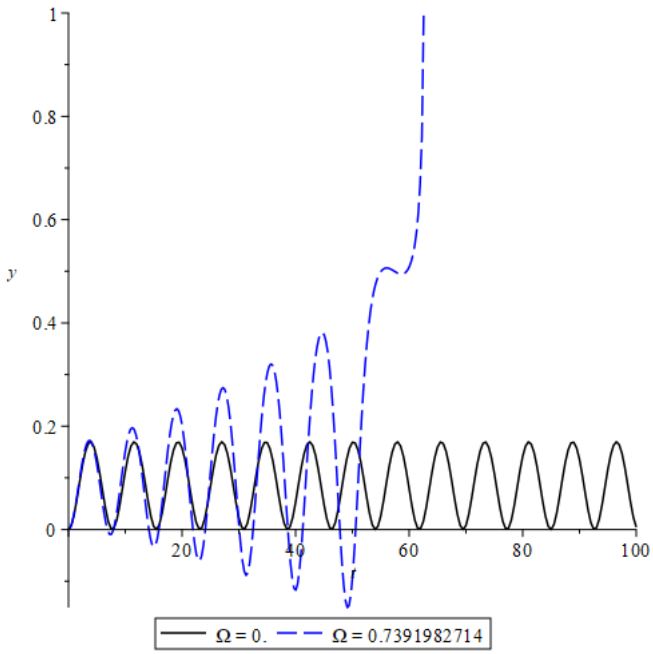

Figure 6-6: Dynamic response of graphene cantilever beam under constant voltage and harmonic excitation at natural angular frequency, $t_{\text{pull-in}} = 62.56$.

Chapter 7

Conclusions and outlooks

In this thesis, a comprehensive analysis of the static and dynamic behavior of a graphene cantilever beam subjected to electrostatic actuation at its free tip was conducted.

Firstly, an analytical solution for the nonlinear static problem was derived, and its consistency with the classical linear solution was demonstrated in the limit where the second-order elastic stiffness constant D approaches zero.

Next, the dynamic pull-in conditions of the system were investigated for two cases: under constant and harmonically excited voltages. Analytical predictions were rigorously validated through numerical simulations presented in Chapter 6. For the case of constant voltage excitation, the system exhibited periodic solutions when the parameter values α and λ lay below the separatix curve, as illustrated in Fig. 5.4. Conversely, pull-in phenomena occurred when these parameters exceeded the separatix curve. The dependency of the deflection amplitude, frequency, and pull-in time on the excitation parameter λ for a fixed value of α was demonstrated in this chapter. Additionally, it was observed that the maximum deflection amplitude occurred just below the separatix value for the given α.

Furthermore, simulations of the cantilever beam under harmonic load excitation revealed that selecting an excitation frequency near the resonant frequency of the beam could lead to structural collapse even though the parametric values were below the pull-in conditions.

Chapter 8

Appendix

Here we show that the analytic solution provided in (3.14) coincides with the classical deflection equation for a cantilever beam under a point load, where the beam is assumed to be a linear elastic material and that the deflection is small compared to the length of the beam. It also assumes that the load is applied perpendicular to the beam's longitudinal axis, and that the beam has a uniform cross-sectional area.

$$\begin{aligned}\lim_{D\to 0} w(x) &= \lim_{D\to 0}\left(\frac{EI}{4DI_2}x^2 - \frac{((EI)^2 - 4DI_2F(x-l))^{\frac{5}{2}}}{120(DI_2)^3F^2} - \frac{((EI)^2+4DI_2Fl)^{\frac{3}{2}}}{12(DI_2)^2F}x\right.\\ &\quad\left. + \frac{((EI)^2+4DI_2Fl)^{\frac{5}{2}}}{120(DI_2)^3F^2}\right)\\ &= \frac{1}{120}\lim_{D\to 0}\left[\frac{30EI(DI_2)^2F^2x^2 - ((EI)^2 - 4DI_2F(x-l))^{5/2}}{(DI_2)^3F^2}\right.\\ &\quad\left. + \frac{-10DI_2F((EI)^2+4DI_2Fl)^{3/2}x + ((EI)^2+4DI_2Fl)^{5/2}}{(DI_2)^3F^2}\right].\end{aligned} \tag{8.1}$$

Replacing some terms of (8.1) with a and b such that

$$a = EI \quad \text{and} \quad b = I_2F, \tag{8.2}$$

then, (8.1) can be simplified as

$$\frac{1}{120}\lim_{D\to 0}\left[\frac{30ab^2D^2x^2-(a^2-4Db(x-l))^{5/2}-10bD(a^2+4Dbl)^{3/2}x+(a^2+4Dbl)^{5/2}}{D^3I_2b^2}\right]. \tag{8.3}$$

Since plugging 0 instead of D in (8.3) gives indeterminate form (i.e. $\left[\frac{0}{0}\right]$), we apply L'Hospital's Rule. Then, we get

$$\begin{aligned}\frac{1}{120}\lim_{D\to 0}\Bigg[&\frac{60ab^2Dx^2+10b(x-l)(a^2-4Db(x-l))^{3/2}-10b(a^2+4Dbl)^{3/2}x}{3D^2I_2b^2}\\&+\frac{-60Db^2l(a^2+4Dbl)^{1/2}+10bl(a^2+4Dbl)^{3/2}}{3D^2I_2b^2}\Bigg].\end{aligned} \tag{8.4}$$

We apply the L'Hospital's Rule again because (8.4) is indeterminate:

$$\begin{aligned}\frac{1}{120}\lim_{D\to 0}\Bigg[&\frac{60ab^2x^2-60b^2(x-l)^2(a^2-4Db(x-l))^{1/2}-120b^2l(a^2+4Dbl)^{1/2}x}{6DI_2b^2}\\&+\frac{-120Db^3l^2(a^2+4Dbl)^{-1/2}x+60b^2l^2(a^2+4Dbl)^{1/2}}{6DI_2b^2}\Bigg].\end{aligned} \tag{8.5}$$

Applying the L'Hospital's Rule one more time yields

$$\begin{aligned}\frac{1}{120}\lim_{D\to 0}\Bigg[&\frac{120b^3(x-l)^3(a^2-4Db(x-l))^{-1/2}-360b^3l^2(a^2+4Dbl)^{-1/2}x}{6I_2b^2}\\&+\frac{240Db^4l^3(a^2+4Dbl)^{-3/2}x+120b^3l^3(a^2+4Dbl)^{-1/2}}{6I_2b^2}\Bigg]\\&=\frac{1}{120}\left[\frac{120b^3(x-l)^3a^{-1}-360b^3l^2a^{-1}x+120b^3l^3a^{-1}}{6I_2b^2}\right]\\&=\frac{bx^3-3blx^2}{6aI_2}.\end{aligned} \tag{8.6}$$

Replacing back a and b, and simplifying the resultant expression we can obtain the following equation

$$\lim_{D\to 0} w(x)=\frac{Fx^2}{6EI}(x-3l), \tag{8.7}$$

which coincides with the classical deflection equation for a cantilever beam under a point load [21].

Bibliography

[1] Naveed Anjum and Ji-Huan He. Nonlinear dynamic analysis of vibratory behavior of a graphene nano/microelectromechanical system. *Mathematical Methods in the Applied Sciences*, 2020.

[2] Alexander A Balandin, Suchismita Ghosh, Wenzhong Bao, Irene Calizo, Desalegne Teweldebrhan, Feng Miao, and Chun Ning Lau. Superior thermal conductivity of single-layer graphene. *Nano letters*, 8(3):902–907, 2008.

[3] Zhong Chen, Umesh Gandhi, Jinwoo Lee, and RH Wagoner. Variation and consistency of young's modulus in steel. *Journal of Materials Processing Technology*, 227:227–243, 2016.

[4] Mai Duc Dai, Chang-Wan Kim, and Kilho Eom. Nonlinear vibration behavior of graphene resonators and their applications in sensitive mass detection. *Nanoscale research letters*, 7:1–10, 2012.

[5] Michael S Fuhrer, Chun Ning Lau, and Allan H MacDonald. Graphene: materially better carbon. *MRS bulletin*, 35(4):289–295, 2010.

[6] Suchismita Ghosh, Irene Calizo, Desalegne Teweldebrhan, Evghenii P Pokatilov, Denis L Nika, Alexander A Balandin, Wenzhong Bao, Feng Miao, and C Ning Lau. Extremely high thermal conductivity of graphene: Prospects for thermal management applications in nanoelectronic circuits. *Applied Physics Letters*, 92(15), 2008.

[7] M S Hanay, S Kelber, AK Naik, D Chi, S Hentz, EC Bullard, E Colinet, L Duraffourg, and ML Roukes. Single-protein nanomechanical mass spectrometry in real time. *Nature nanotechnology*, 7(9):602–608, 2012.

[8] Matthew A Hopcroft, William D Nix, and Thomas W Kenny. What is the young's modulus of silicon? *Journal of microelectromechanical systems*, 19(2):229–238, 2010.

[9] Alastair Macrae Howatson. *Engineering tables and data*. Springer Science & Business Media, 2012.

[10] Francesca Iacopi, SH Brongersma, Bart Vandevelde, M O'Toole, D Degryse, Y Travaly, and K Maex. Challenges for structural stability of ultra-low-k-based interconnects. *Microelectronic engineering*, 75(1):54–62, 2004.

[11] K Jensen, Kwanpyo Kim, and A Zettl. An atomic-resolution nanomechanical mass sensor. *Nature nanotechnology*, 3(9):533–537, 2008.

[12] Shirali Kadyrov, Ardak Kashkynbayev, Piotr Skrzypacz, Konstantinos Kaloudis, and Anastassios Bountis. Periodic solutions and the avoidance of pull-in instability in nonautonomous microelectromechanical systems. *Mathematical Methods in the Applied Sciences*, 44(18):14556–14568, 2021.

[13] Danilo Karličić, Predrag Kozić, Sondipon Adhikari, Milan Cajić, Tony Murmu, and Mihailo Lazarević. Nonlocal mass-nanosensor model based on the damped vibration of single-layer graphene sheet influenced by in-plane magnetic field. *International Journal of Mechanical Sciences*, 96:132–142, 2015.

[14] Zulfiqar H Khan, Atieh R Kermany, Andreas Öchsner, and Francesca Iacopi. Mechanical and electromechanical properties of graphene and their potential application in mems. *Journal of Physics D: Applied Physics*, 50(5):053003, 2017.

[15] Changgu Lee, Xiaoding Wei, Jeffrey W Kysar, and James Hone. Measurement of the elastic properties and intrinsic strength of monolayer graphene. *science*, 321(5887):385–388, 2008.

[16] Jae-Ung Lee, Duhee Yoon, and Hyeonsik Cheong. Estimation of young's modulus of graphene by raman spectroscopy. *Nano letters*, 12(9):4444–4448, 2012.

[17] Ying Li. Reversible wrinkles of monolayer graphene on a polymer substrate: toward stretchable and flexible electronics. *Soft matter*, 12(13):3202–3213, 2016.

[18] Qiang Lu and Rui Huang. Nonlinear mechanics of single-atomic-layer graphene sheets. *International Journal of Applied Mechanics*, 1(03):443–467, 2009.

[19] Toshiaki Natsuki, Jin-Xing Shi, and Qing-Qing Ni. Vibration analysis of nanomechanical mass sensor using double-layered graphene sheets resonators. *Journal of Applied Physics*, 114(9), 2013.

[20] Daniyar Omarov, Daulet Nurakhmetov, Dongming Wei, and Piotr Skrzypacz. On the application of sturm's theorem to analysis of dynamic pull-in for a graphene-based mems model. *Applied and computational mechanics*, 12(1), 2018.

[21] Joseph Edward Shigley, Larry D Mitchell, and H Saunders. Mechanical engineering design. 1985.

[22] Piotr Skrzypacz, Anastasios Bountis, Daulet Nurakhmetov, and Jong Kim. Analysis of the lumped mass model for the cantilever beam subject to grob's swelling pressure. *Communications in Nonlinear Science and Numerical Simulation*, 85:105230, 2020.

[23] Piotr Skrzypacz, Shirali Kadyrov, Daulet Nurakhmetov, and Dongming Wei. Analysis of dynamic pull-in voltage of a graphene mems model. *Nonlinear Analysis: Real World Applications*, 45:581–589, 2019.

[24] Piotr Skrzypacz, Dongming Wei, Daulet Nurakhmetov, Eduard G Kostsov, Alexei A Sokolov, Madi Begzhigitov, and Grant Ellis. Analysis of dynamic pull-in voltage and response time for a micro-electro-mechanical oscillator made of power-law materials. *Nonlinear Dynamics*, 105:227–240, 2021.

[25] Gary A Steele, Andreas K Hüttel, Benoit Witkamp, Menno Poot, Harold B Meerwaldt, Leo P Kouwenhoven, and Herre SJ van der Zant. Strong coupling between single-electron tunneling and nanomechanical motion. *Science*, 325(5944):1103–1107, 2009.

[26] Hikari Tomori, Akinobu Kanda, Hidenori Goto, Youiti Ootuka, Kazuhito Tsukagoshi, Satoshi Moriyama, Eiichiro Watanabe, and Daiju Tsuya. Introducing nonuniform strain to graphene using dielectric nanopillars. *Applied physics express*, 4(7):075102, 2011.

[27] Vijay K Varadan, Kalarickaparambil Joseph Vinoy, and K Abraham Jose. *RF MEMS and their applications*. John Wiley & Sons, 2003.

[28] Xiaomu Wang, He Tian, Weiguang Xie, Yi Shu, Wen-Tian Mi, Mohammad Ali Mohammad, Qian-Yi Xie, Yi Yang, Jian-Bin Xu, and Tian-Ling Ren. Observation of a giant two-dimensional band-piezoelectric effect on biaxial-strained graphene. *NPG Asia Materials*, 7(1):e154–e154, 2015.

[29] Dongming Wei, Yu Liu, and Mohamad B Elgindi. Some analytic and finite element solutions of the graphene euler beam. *International Journal of Computer Mathematics*, 91(10):2276–2293, 2014.

[30] Dongming Wei, Daulet Nurakhmetov, Almir Aniyarov, Dichuan Zhang, and Christos Spitas. Lumped-parameter model for dynamic monolayer graphene sheets. *Journal of Sound and Vibration*, 534:117062, 2022.

[31] Seishi Yajima, Kiyohito Okamura, and Josaburo Hayashi. Structural analysis in continuous silicon carbide fiber of high tensile strength. *Chemistry Letters*, 4(12):1209–1212, 1975.

[32] Mohammad I Younis. *MEMS linear and nonlinear statics and dynamics*, volume 20. Springer Science & Business Media, 2011.